


Article

Subseasonal Influences of Teleconnection Patterns on the Boreal Wintertime Surface Air Temperature over Southern China as Revealed from Three Reanalysis Datasets

Ning Shi ^{1,*} , Dongdong Zhang ², Yicheng Wang ² and Suolang Tajie ²

¹ Collaborative Innovation Center on Forecast and Evaluation of Meteorological Disasters, Key Laboratory of Meteorological Disasters of the Ministry of Education, Nanjing University of Information Science and Technology, Nanjing 210044, China

² College of Atmospheric Science, Nanjing University of Information Science and Technology, Nanjing 210044, China

* Correspondence: shining@nuist.edu.cn

Received: 31 July 2019; Accepted: 29 August 2019; Published: 1 September 2019



Abstract: The daily fields from three reanalysis datasets are utilized to explore the subseasonal influence of teleconnection patterns on the surface air temperature (SAT) over southern China. Due to the similarity of the results from the different datasets, the ensemble mean is then used in this study. After applying the false discovery rate to the significance test, the composite results reveal that positive Western Pacific (WP) events, East Atlantic (EA) events, Scandinavian (SCA) events, and Eastern Atlantic/Western Russia (EAWR) events are the teleconnection events that have an influence on SAT anomalies over southern China. The timing of inducing significant SAT anomalies over southern China is similar among positive WP events, EA events and EAWR events, i.e., approximately the first 5-day period after their peak day. In contrast, SCA events exert a lagged significant influence on SAT, i.e., during approximately the second 6-day period after their peak day. Therefore, considering that significant circulation anomalies generally begin to appear at least 4 days before the peak day, these teleconnection events could be used as subseasonal predictors for SAT anomalies over southern China.

Keywords: teleconnection patterns; southern China; subseasonal timescale

1. Introduction

Extratropic teleconnection patterns in the Northern Hemisphere were first systematically proposed by Wallace and Gutzler [1] through the grid point-based correlation coefficients of the monthly 500 hPa geopotential height (Z500), i.e., Western Atlantic, East Atlantic (EA), Eurasian (EU), Pacific/North American (PNA), and Western Pacific (WP) patterns. By using rotated principal component analysis (RPCA) on the monthly 700 hPa geopotential height, Horel [2] and Barnston and Livezey [3] proposed nine winter teleconnection patterns in the Northern Hemisphere: North Atlantic oscillation (NAO), EA, EU type 1, EU type 2, Northern Asian, WP, Eastern Pacific (EP), PNA, and tropical/Northern Hemisphere. In addition, by applying the empirical orthogonal function to the root mean square statistics of bandpass-filtered geopotential height [4] or the daily zonal wind field [5] over the North Pacific and North Atlantic, some extratropic teleconnection patterns could also be identified, e.g., PNA, WP, NAO, and EA.

Teleconnection patterns are characterized by their planetary spatial scale and by the “seesaw” and/or wavelike structures in the horizontal direction at a monthly or seasonal mean timescale [6,7]. Previous studies have revealed that energy extraction from the background flow [7–11], quasi-stationary

Rossby wave propagation [12–14], transient eddy feedback forcing [4,13,14], and the interaction between low-frequency circulation anomalies and background flow [15,16] are regarded as fundamental mechanisms for the formation and maintenance of teleconnection patterns.

Due to the hemispheric or regional influence of teleconnection patterns on the weather and climate, the Climate Prediction Center (CPC) of the National Weather Service (<https://www.cpc.ncep.noaa.gov>) offers monthly indices for those teleconnection patterns, which are mainly based on the RPCA method [3]. On the website, the two types in the EU in [3] are referred to as the Scandinavian (SCA) and East Atlantic/West Russia (EAWR) patterns. This terminology will be used in the present study.

Southern China is subject to cold surges originating from mid-latitude Eurasia, and it is also a region where the variability of surface air temperature (SAT) is evident [17–19]. Based on seasonal mean or monthly mean data, some studies have revealed that both the conventional EU pattern and the WP pattern are significantly correlated with the East Asia winter monsoon and the surface air temperature over southern China [20–23]. Note that the *e*-folding timescale of teleconnection patterns is generally 7–10 days [24,25], indicating a lifecycle of 2–3 weeks. On the other hand, the typical evolution of a cold surge over East Asia occurs over a period of 2–3 weeks [17,26]. Such a coincidence between the lifecycles of teleconnection patterns and that of the cold surge inspired us to explore whether teleconnection patterns could exert a significant influence on the SAT over southern China on the subseasonal timescale.

In fact, on the subseasonal timescale, Wang and Zhang [16] revealed that significant negative (positive) SAT anomalies over southern China could be observed 2 to 4 days after the peak day of the conventional positive (negative) EU pattern [1]. Note that both the SCA and EAWR patterns, which are the two types of EU pattern, are slightly different from the conventional EU patterns [27] in the position of their centers of action, implying that they have different influences than the conventional EU patterns. It seems that the SCA could act as a precursory signal at least one week before the occurrence of cold SAT anomalies over southern China. For example, Zhou et al. [28] and Bueh et al. [29] noticed that positive SCA was evident in December 2017, which was prior to the occurrence of persistent low temperature and icy weather over southern China one month later. Moreover, after examining 24 persistent extreme cold events over China that occurred from 1951 through 2009, Peng et al. [30] found that 10 days before the peak day of persistent extreme cold events, a southwest–northeast-oriented tilted ridge at 500 hPa formed around the Europe–Barents Sea, indicating the occurrence of the SCA pattern. As for the EAWR pattern, Liu et al. [27] demonstrated that the influence of the winter mean EAWR pattern on the SAT over East Asia was mainly confined to north of 40° N, exerting no significant influence on the SAT over southern China. In fact, the cold surges or SAT anomalies that form around Lake Baikal generally propagate along the northeastern slope of the Tibetan Plateau before they arrive at southern China [17,26,31]. Therefore, if the SAT anomalies form to the north of the Tibetan Plateau, as revealed by Liu et al. [27], they might influence the SAT over southern China through southeastward propagation. Thus, it is worth elucidating whether the SCA and EAWR patterns could significantly influence the SAT over southern China on the subseasonal timescale.

Takaya et al. [18,19] showed that the blocking high over the northwestern Pacific could displace westward to the Far East and further enhance the Siberian high, leading to cold air outbreak over southern China. Their studies imply that on the subseasonal timescale the positive WP could influence the SAT over East Asia (including southern China), which is discussed in the present study. Moreover, considering the planetary spatial scale of the teleconnection patterns, it is also worth studying whether other dominant teleconnection patterns could significantly influence the SAT over southern China.

2. Data and Methods

2.1. Data and Processing

The present study used three reanalysis datasets: (1) European Centre for Medium-Range Weather Forecasts interim reanalysis (ERA-interim) [32] from 1 January 1979 to 31 March 2019; (2) National

Centers for Environmental Prediction and National Center for Atmospheric Research (NCEP/NCAR) reanalysis [33] from 1 January 1948 to 31 March 2019; and (3) Japanese 55-year reanalysis (JRA) from 1 January 1958 to 31 March 2019 [34]. The horizontal resolutions for the three reanalysis datasets are 1.5° , 2.5° , and 1.25° , respectively. As shown in Section 3.1, the results obtained from different datasets are similar to a great extent; thus, the ensemble mean of the three datasets was used in our analysis. Before taking the ensemble mean, the bilinear interpolation procedure was applied to the ERA and JRA datasets to obtain the same horizontal resolution of 2.5° as that of the NCEP/NCAR reanalysis dataset. Variables included Z500, SAT, and sea level pressure (SLP). In addition, the monthly fields from the three reanalysis datasets were used to obtain the teleconnection patterns and their monthly influence on the surface climate. Due to the large uncertainty of the NCEP/NCAR reanalysis before the 1970s, especially in the lower troposphere over the Asian continent [35], only the period from 1 January 1970 to 31 March 2019 is analyzed.

The monthly mean standardized Z500 anomalies were calculated for the 40 winters from 1979–1980 to 2018–2019. The winter season was defined as the 5 months from November through March. For example, winter 2000 refers to November 2000 through March 2001. In a particular calendar month, the Z500 anomalies were obtained and further standardized by the 40-year period monthly means and standard deviations. The 40-year period was the common period for the three reanalysis datasets; thus, the analysis of this common period facilitated the comparison of teleconnection patterns among the datasets and verify their robustness. The data sequences of JRA and NCEP/NCAR before 1979 were also analyzed for the discussion of decadal variation.

The daily standardized Z500 anomalies were used to calculate the daily indices of the teleconnection patterns. The daily anomalies were first obtained by subtracting the climatological seasonal cycle from the raw daily fields. The climatological seasonal cycle was defined as the 31-day running mean of daily climatology. The daily anomalies were further standardized by the standard deviation of the corresponding day. For a particular calendar day, the standard deviation was obtained by the 31-day period centered around that day spanning 40 years, i.e., $31 \text{ days/year} \times 40 \text{ years} = 1240 \text{ days}$.

2.2. Methods

2.2.1. Teleconnection Patterns

The method used in CPC to obtain the teleconnection patterns was used here, but with minor modifications. The method is based on RPCA used by Barnston and Livezey [3] and applied to the three reanalysis datasets. The following is a brief description: First, the 10 leading unrotated empirical orthogonal functions are determined from the monthly standardized Z500 height anomalies in the region $20\text{--}90^\circ \text{ N}$ with the temporal sequence $40 \text{ years} \times 5 \text{ months/year} = 200 \text{ months}$. Then, the Kaiser varimax rotation is applied to these 10 leading unrotated modes, yielding the 10 leading rotated modes and corresponding time series.

2.2.2. Daily Indices of Teleconnection Patterns

The daily indices of the teleconnection patterns were obtained by projecting the standardized daily Z500 anomalies to the teleconnection patterns, which is similar to the method used by Baldwin and Dunkerton [36] to calculate the daily Arctic oscillation index. The daily index for each teleconnection pattern was further normalized locally by the standard deviation of the daily index over $31 \text{ days/year} \times 40 \text{ years} = 1240 \text{ days}$, where the annual 31-day sequence is centered on that calendar day. Based on these daily indices, the teleconnection pattern events were picked out. Taking a positive WP event as an example, it can be identified if (1) the WP index value at the peak day exceeds 1.5 standard deviation; (2) the WP index values on its start and end days exceed 0.5 standard deviation and the duration is no less than 5 days; and (3) the interval of the peak day for 2 adjacent positive WP events is larger than 20 days.

2.2.3. Effective Sample Size

In the significance test of the linear correlation coefficients, the autocorrelation of the daily time series was used to evaluate the effective sample size $N^* = N \times (1 - r_1 r_2) / (1 + r_1 r_2)$. N is the original length of the series, and r_1 and r_2 are the lag-one autocorrelation coefficients of the two time series involved in the correlation analysis.

2.2.4. Significance Test

The statistical significance of our results was tested based on 2-tailed Student's t test at each grid point. The false discovery rate (FDR) [37] was applied to the significance test in this study to effectively control the proportion of falsely rejected null hypotheses. The threshold value for the significance level, p_{FDR}^* , was determined based on the distribution of ascending sorted p values:

$$p_{\text{FDR}}^* = \max_{i=1, \dots, N} [p_{(i)} \leq (i/N)\alpha_{\text{FDR}}] \quad (1)$$

where $p_{(i)}$ is the i -th smallest p value of all p values evaluated at each grid point of a composite or regression map, N is the total number of grid points, and the control level for the FDR, α_{FDR} , is set as 0.05.

3. Results

3.1. Comparison of Teleconnection Patterns Revealed by Different Datasets

The three reanalysis datasets consistently reveal that there are nine dominant teleconnection patterns in the Northern Hemisphere, as obtained from the 10 leading rotated modes. These patterns are WP, NAO, PNA, polar/Eurasia (PE, referred to as the Northern Asia pattern in Barnston and Livezey [3]), EA, SCA, tropical/Northern Hemisphere (TNH), East Pacific–North Pacific (EPNP), and EAWR. The nine patterns are consistent with those monitored by CPC. The remaining spurious mode, which mainly shows consistent variation over the mid and lower latitudes, is not documented by the previous studies and seems to have no apparent physical meaning. Thus, the discussion will be focused only on the nine dominant teleconnection patterns. As for the conventional EU pattern proposed in [1], it is generally defined by the Z500 anomalies at three particular grid points rather than by RPCA. In fact, our study did not identify this conventional EU pattern during the period 1979 to 2018 based on any of the three reanalysis datasets, which is consistent with Barnston and Livezey [3] and the CPC. Thus, the influence of the EU pattern is not discussed in the present study.

Before showing the spatial patterns of the nine teleconnection patterns in Section 3.2, we would like to compare the patterns from different reanalysis datasets in terms of priority. Table 1 shows some statistics for the nine patterns. Both the ranking and explained variance of each teleconnection pattern generally have little difference among the three datasets, except for the evident higher explained variance for NAO in ERA-interim. The e -folding timescales for the nine teleconnection patterns are also shown in Table 1. The e -folding timescale is determined by the day when the lagged autocorrelation coefficients reduce to $1/e$. Clearly, the reanalysis datasets show almost the same results. NAO, PNA, and PE tend to have the longest e -folding timescales, approximately 9 days, while TNH, EPNP, and EAWR have the shortest, approximately 6 days. The e -folding timescale for WP is 7 days in both ERA-interim and JRA, and 8 days in NCEP/NCAR. Feldstein [24] stated that NAO and WP have 9.5-day and 7.4-day e -folding timescales, respectively. Thus, our results are basically consistent with Feldstein [24]. In addition, the spatial correlation coefficients generally exceed 0.9 for every teleconnection pattern between any pair of reanalysis datasets (not shown). Based on the similarities in the above-mentioned statistics, the ensemble mean of the three reanalysis datasets will be used in the following.

Table 1. Explained variance S_{exp}^2 (%) of the principal component time series, and ranking and e -folding timescale τ (days) for the nine teleconnection patterns obtained from three reanalysis datasets over the winter periods from 1979 to 2018.

	EM			ERA-Interim			JRA			NCEP/NCAR		
	Mode	S_{exp}^2	τ	Mode	S_{exp}^2	τ	Mode	S_{exp}^2	τ	Mode	S_{exp}^2	τ
NAO	1	8.52	9	2	8.59	9	4	7.53	9	4	7.69	9
WP	3	8.21	7	1	8.59	7	1	8.79	8	2	8.26	7
PNA	4	7.90	9	4	7.66	9	3	7.87	9	3	7.94	10
PE	5	6.64	9	5	6.91	9	5	7.11	9	5	7.12	9
EA	6	6.41	8	7	6.12	8	7	6.15	8	8	6.02	7
SCA	7	6.31	7	6	6.48	7	6	6.39	7	7	6.12	7
TNH	8	5.77	6	8	5.87	6	8	6.13	6	6	6.12	6
EPNP	9	5.29	6	10	5.17	6	10	5.06	7	10	5.11	6
EAWR	10	4.98	6	9	5.25	6	9	5.21	6	9	5.36	6

EM, ensemble mean; ERA-interim, European Centre for Medium-Range Weather Forecasts interim; JRA, Japanese 55-year reanalysis; NCEP/NCAR, National Centers for Environmental Prediction and National Center for Atmospheric Research; NAO, North Atlantic oscillation; WP, Western Pacific; PNA: Pacific/North American; PE, polar/Eurasia; EA, East Atlantic; SCA, Scandinavian; TNH, tropical/Northern Hemisphere; EAWR, East Atlantic/West Russia.

To further explore whether the ensemble mean could represent the three reanalysis datasets or not, Table 1 also shows the statistics based on the ensemble mean. Evidently, the results on both the explained variance and e -folding timescales have little difference with any of the three reanalysis datasets. Our final results are not sensitive to slight differences in the rankings of the patterns from different datasets (Table 1), since it is the daily indices of the teleconnection patterns that are the bases for the identification of teleconnection events. Table 2 shows the linear correlation coefficients between the daily indices of the nine dominant teleconnection patterns based on the ensemble mean and the three reanalysis datasets over the 40-year winter period. Clearly, the correlation coefficients are generally higher than 0.9 during the 40-year period, except for the correlation coefficient of 0.838 for the EPNP between the ensemble mean and the JRA datasets. Such high correlation coefficient values indicate that the ensemble mean is representative of all three reanalysis datasets. Therefore, the following shows only the results based on ensemble mean rather than similar results based on different reanalysis datasets.

Table 2. Linear correlation coefficients r between daily indices of nine teleconnection patterns based on ensemble mean and the three reanalysis datasets over the winter periods from 1979 to 2018. All coefficients are significant at the $\alpha = 0.05$ confidence level.

	r (EM, ERA)	r (EM, JRA)	r (EM, NCEP/NCAR)
NAO	0.996	0.992	0.993
WP	0.995	0.992	0.997
PNA	0.996	0.965	0.985
PE	0.994	0.993	0.994
EA	0.991	0.936	0.942
SCA	0.996	0.980	0.993
TNH	0.982	0.979	0.987
EPNP	0.921	0.838	0.933
EAWR	0.989	0.910	0.931

3.2. Relationship with Area-Averaged SAT Over Southern China

Figure 1 shows the spatial patterns of the nine teleconnection patterns based on the ensemble mean of the three reanalysis datasets. The patterns are represented by the regression coefficients of the monthly Z500 anomalies on the normalized rotated principal component time series. In the present

study, the positive phase of these patterns is defined as when the regression coefficient averaged over the polar region (north of 60° N) is positive. NAO and WP mainly exhibit meridional dipole patterns over the North Atlantic and the North Pacific, respectively (Figure 1a,b). PNA (Figure 1c) and TNH (Figure 1g) exhibit similar wave train anomalies from the North Pacific to the North Atlantic via northern North America, but the anomaly centers of action are located at different geographic locations for these two patterns. PE (Figure 1d) consists of height anomalies with the same sign over the polar region, northern China, and Mongolia. EA (Figure 1e), SCA (Figure 1f), and EAWR (Figure 1i) consist of wave train anomalies over different regions of the mid- and high-latitude Eurasian continent. EA and EAWR are also characterized by significant Z500 anomalies over the North Atlantic. EPNP (Figure 1h) primarily consists of two anomaly centers of action over the Bering Strait and Greenland and three anomaly centers of action with the opposite sign over the central North Pacific, eastern Canada, and northeastern North Atlantic/Western Europe.

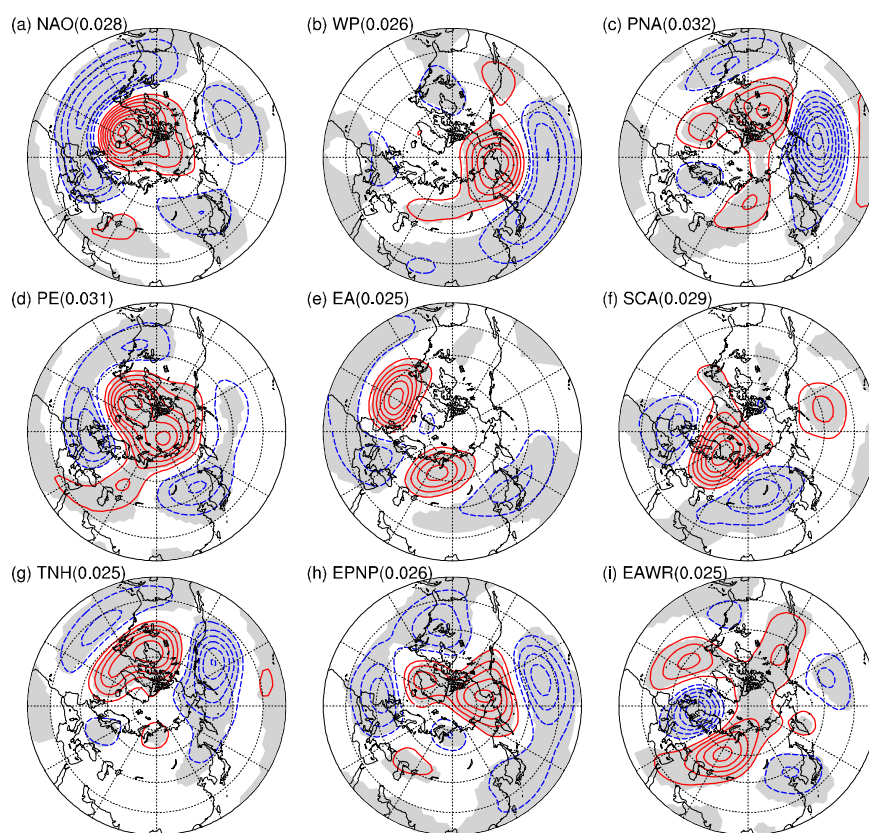


Figure 1. (a–i) Spatial patterns of the nine teleconnection patterns represented by linear regression coefficients of monthly 500 hPa geopotential height (Z500) anomalies on the normalized rotated principal component analysis (RPCA) time series during the 40 winters from 1979 to 2018, based on the ensemble mean of the three reanalysis datasets. Name of each teleconnection pattern is indicated in top left of the corresponding panel. Shading denotes significant anomalies based on two-tailed Student's t test controlled by false discovery rates with $\alpha_{\text{FDR}}^* = 0.05$. Threshold values for the significance level, p_{FDR}^* , are shown in the top left of each panel. Contours are drawn for $\pm 50, \pm 100, \dots$, m. Solid red and dashed blue lines represent positive and negative anomalies, respectively.

To facilitate the discussion on the relationship between teleconnection patterns and SAT anomalies, Figures 2 and 3 show the composite SAT anomaly area-averaged over southern China ($110\text{--}120^\circ$ E, $25\text{--}40^\circ$ N) during the evolution of teleconnection pattern events. Hereafter, the peak day is referred to as the reference day and denoted as day 0, while days $-N$ and N refer to the composite N days before and after the peak day, respectively.

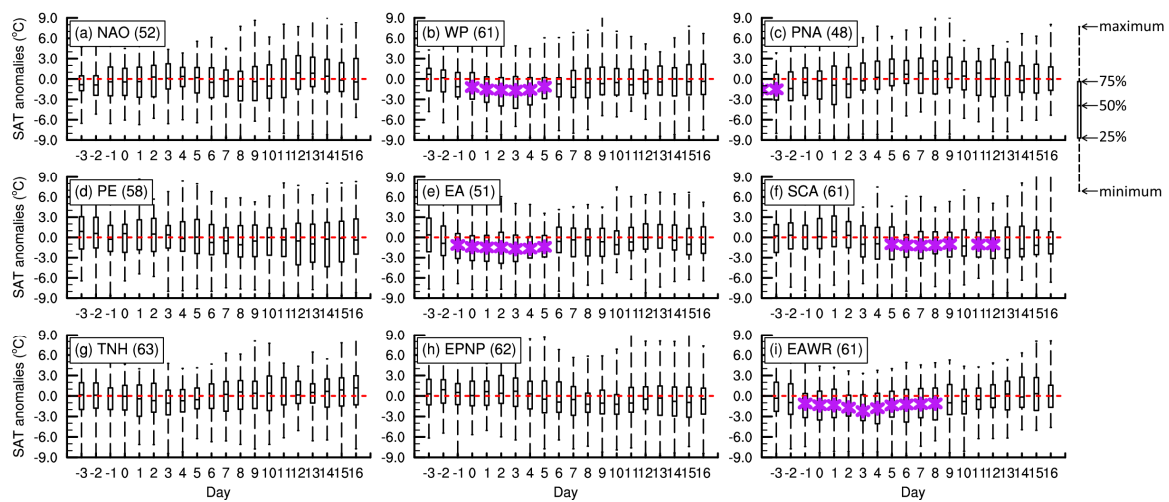


Figure 2. (a–i) Boxplots of daily SAT anomalies averaged over eastern China during the evolution of nine teleconnection patterns in their positive phases during the 40 winters from 1979 to 2018. Abscissas represent days relative to the peak day of the teleconnection pattern. Purple asterisks represent composite anomalies that are significant at the 0.05 level, based on two-tailed Student’s *t* test controlled by false discovery rates of each teleconnection pattern is indicated in top-right of the corresponding panel. Name and numbers in top-left of panels indicate the name of teleconnection pattern and number of cases used for the composite analysis, respectively.

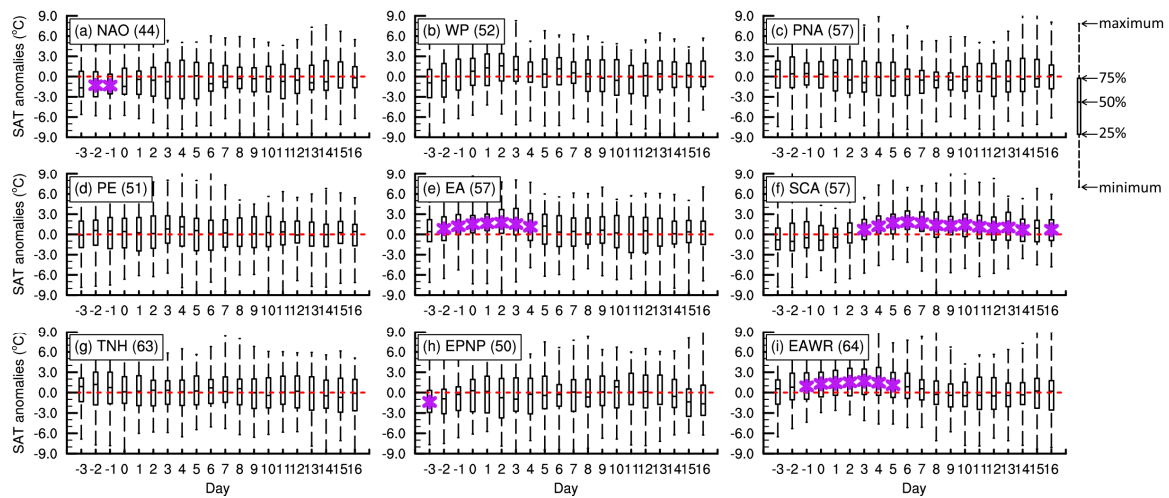


Figure 3. (a–i) Same as subfigures (a–i) of Figure 2, respectively, but in the negative phase of the nine teleconnection patterns.

Clearly, not every type of teleconnection event is accompanied by significant SAT anomalies over southern China. If significant SAT anomalies persisting for at least three consecutive days are considered as having an effective influence on the teleconnection patterns, only the WP events in their positive phase (Figure 2b), the EA events (Figures 2e and 3e), the SCA events (Figures 2f and 3f), and the EAWR events (Figures 2i and 3i) are influential in the formation of SAT anomalies over southern China. Note that significant and persistent SAT anomalies generally occur after the peak days. Specifically, the significant negative SAT anomaly persists from day 0 through day 5 for the positive WP events (Figure 2b) and from day –1 to day 5 for the positive EA events (Figure 2e), and the significant negative SAT anomaly persists from day –2 to day 4 for the negative EA events (Figure 3e) and from day –1 to day 5 for the negative EAWR events (Figure 3i). Therefore, SAT anomalies tend to persist for 5 to 6 days after the peak days of the four types of teleconnection events. The negative SAT anomaly exhibits longer persistence for the positive EAWR events, i.e., from day –1 to day 8 (Figure 2i). Interestingly, the

SCA events tend to be accompanied by significant SAT anomalies with a larger lag than other events. For example, significant negative SAT anomalies occur from day 5 to day 12 with an interruption at day 10 for the positive SCA events (Figure 2f), and from day 3 to day 16 with an interruption at day 15 (Figure 2f). Therefore, significant SAT anomalies over southern China tend to occur approximately at the second 6-day period after the peak day of SCA events, while they occur approximately at the first 5-day period after the peak day of positive WP events, EA events, and EAWR events.

The above-mentioned significant composite results never imply that all cases exhibit the same results. In fact, some cases even exhibit an opposite value to the composite mean value. Therefore, to further understand the significant composite results, the minimum, first quartile, median, third quartile, and maximum values are also shown in the boxes in Figures 2 and 3. Overall, significant SAT anomalies correspond to approximately 75% of the teleconnection events with the same sign as SAT anomalies over southern China. Taking a particular positive WP event as an example, there is a 75% probability that the event could be followed by a negative SAT anomaly during the first 5-day period after the peak day. Thus, the significant composite results could be used as a good reference for operational forecasting of SAT anomalies over southern China.

Overall, positive WP events, SCA events, EA events, and EAWR events could act as precursory circulation signals for SAT anomalies over southern China. Interestingly, the one-week interval between the peak day of SCA events and significant SAT anomalies is evidently longer than the intervals of the other teleconnection patterns.

3.3. Circulation Evolution

As discussed in the previous section, significant and persistent area-averaged SAT anomalies over southern China generally occur after the peak days of positive WP, EA events, SCA events and EAWR events. The following will focus on these events. To better understand the reason for the formation of significant SAT anomalies, we still need to explore the related evolution features of circulation anomalies. For the sake of brevity, the daily evolutions of WP, EA, SCA, and EAWR events only in their positive phases are discussed in the following, since the events in the negative phase exhibit similar evolution to their positive counterparts but with the opposite sign except for the negative WP events (not shown). The features in the negative phase of the teleconnection patterns will be briefly discussed.

3.3.1. WP Events

A significant dipole of Z500 anomalies appeared over the northern Pacific at day -8 (not shown), with the positive center of action over the Aleutian Islands and the negative center to the north of the Hawaii Islands. The anomaly dipole gradually moved westward, and the negative Z500 anomalies gradually merged with the negative anomalies over the western Pacific. At day -2 , the Far East and southern China began to be influenced by significant positive and negative Z500 anomalies, respectively (Figure 4a). Significant dipole SLP anomalies occurred over the central North Pacific (Figure 4f). The positive SLP anomaly around Bering Strait was favorable for advecting the cold (warm) air mass southward (northward), contributing to the formation of significant warm SAT anomalies over the Far East and the cold anomaly over northwestern North America (Figure 4k). At day 0, circulation anomalies continuously moved westward. As pointed out by Takaya et al. [19], anticyclonic anomalies from the North Pacific could move westward to form a blocking ridge over northeastern Asia, which could induce the enhancement of Siberian high and cold air outbreak over East Asia after the SAT anomaly reaches the northeastern slope of the Tibetan Plateau. Consistent with their study, significant positive SLP anomalies were observed to the north of Lake Baikal at day 0 and day 2 (Figure 4g,h), indicating an enhanced Siberian high, and negative SAT anomalies first formed over northern China (Figure 4l) and the western North Pacific at day 2 (Figure 4m), then propagated southward to influence southern China at day 3 (not shown) and day 4 (Figure 4n). At day 6, the positive Z500 anomalies over the Far East weakened to a large extent and became insignificant (Figure 4e). Correspondingly,

both the SLP anomaly over Eurasia (Figure 4j) and the SAT anomalies over southern China (Figure 4o) were insignificant.

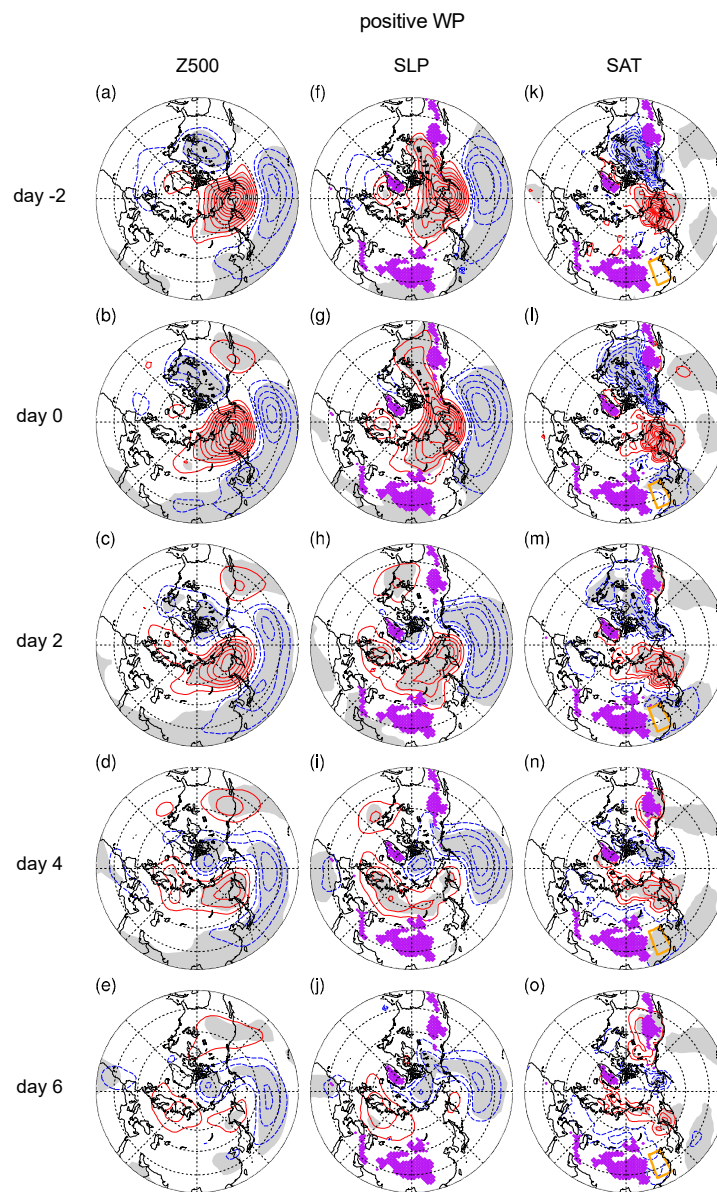


Figure 4. Composites of anomalous Z500 (first column), sea level pressure (SLP) (second column), and SAT (third column) for 61 positive WP events. Shading denotes significant anomalies, based on two-tailed Student's *t* test controlled by false discovery rates with $\alpha_{\text{FDR}}^* = 0.05$. Threshold values for the significance level p_{FDR}^* are 0.008, 0.007, and 0.005 for the composites of anomalous Z500, SLP, and SAT, respectively. Contours are drawn for (a–e) $\pm 25, \pm 50, \dots$ gpm; (f–j) $\pm 2, \pm 4, \dots$ hPa; and (k–o) $\pm 0.5, \pm 1, \dots$ K. Solid red and dashed blue lines represent positive and negative anomalies, respectively. Purple stippling indicates topographic height exceeding 1500 m. Orange rectangles in third column represent southern China.

As for negative WP events (not shown), the Z500 anomalies also exhibited westward movement to the Far East. However, negative SLP anomalies were mainly limited to the northeast of Lake Baikal, and significant SAT anomalies did not form to the northeast of the Tibetan Plateau. Therefore, the southeastward propagation of positive SAT anomalies could not be observed during the negative WP events.

Note that during the evolution of WP events, the evident meridional dipole pattern of SLP anomalies over the North Pacific (Figure 4f–h) had a strong resemblance to the North Pacific oscillation (NPO) [38,39]. To explore whether WP events are related to the NPO, the daily NPO index is calculated by the difference between the normalized SLP anomaly at (65° N, 170° E) and that at (25° N, 165° E), following the results of Wallace and Gutzler [1], but here based on daily data. Like the daily indices of other teleconnection patterns, the NPO index is normalized locally by the standard deviation of daily index over 31 days/year \times 40 years = 1240 days. The linear correlation coefficient between the two indices over the 40 winters (151 days/year \times 40 years = 6040 days) is 0.69, which is significant at the 99% confidence level with an effective sample size of 492. In addition, we also compared the evolution features of the WP and NPO indices during the evolution of WP events. The results show that the evolution features of the two indices match quite well, except for the stronger values of the WP index (not shown). Therefore, although the NPO is defined with the SLP field and the WP is defined with the Z500 field, the WP is closely related to the NPO, which is consistent with Linkin and Nigam [40], who pointed out that the upper-air geopotential height signature of NPO is the WP pattern and NPO/WP constitutes a prominent mode of winter mid-latitude variability.

3.3.2. EA Events

Positive EA events are characterized by a primary anticyclonic Z500 anomaly over the northern Atlantic and wave train anomalies across mid- and high-latitude Eurasia at day 0 (Figure 5b), consistent with Figure 1e. In fact, the primary anticyclonic Z500 anomaly becomes significant at day -6 , while the wave train anomalies become significant at day -4 (not shown). In other words, the typical circulation of positive EA events is significant at day -4 . From day -4 to day 0 (Figure 5a,b), the Z500 anomalies are gradually enhanced. In accordance with the Z500 anomalies, the positive SLP anomalies anchor over the northern North Atlantic and around the Ural Mountains. Since the center of the climatological mean Siberian high is located around Lake Baikal, the positive SLP anomalies indicate enhancement of the northwestern part of the Siberian high, which facilitates the formation of a dipole pattern of SAT anomalies with the warm anomaly around the Kara Sea and the cold one over mid-latitude Eurasia (Figure 5k,l).

From day 0 to day 4 (Figure 5c,d), the typical circulation anomalies of positive EA events gradually weaken. Note that the cold SAT anomaly over mid-latitude Eurasia gradually propagates southeastward along the northeastern slope of the Tibetan Plateau after day -2 (Figure 5k). Southern China is gradually influenced by the significant cold SAT anomaly, especially at day 4 (Figure 5n), which is basically consistent with the persistence of the significant area-averaged SAT anomalies from day -1 to day 5 (Figure 2e). At day 6 (Figure 5e), only the negative Z500 anomaly over northern North Africa/western Europe and the positive Z500 anomaly around the Ural Mountains remain significant, indicating the end of positive EA events. The SAT anomaly is insignificant over southern China after day 6 (Figure 5o).

Unlike WP events, negative EA events show a high similarity to their positive counterparts but with the opposite signs (not shown). The positive SAT anomaly over mid-latitude Eurasia also propagates southeastward along the northeastern slope of the Tibetan Plateau, and influences southern China from approximately day -2 to day 4, basically consistent with the persistence of the significant area-averaged SAT anomalies from day -2 to day 4 (Figure 3e). The southeastward propagation of SAT anomalies along the large-scale topography was revealed by Hsu [31] through linear correlation results. Section 4 briefly discusses the dynamic reason for this southeastward propagation.

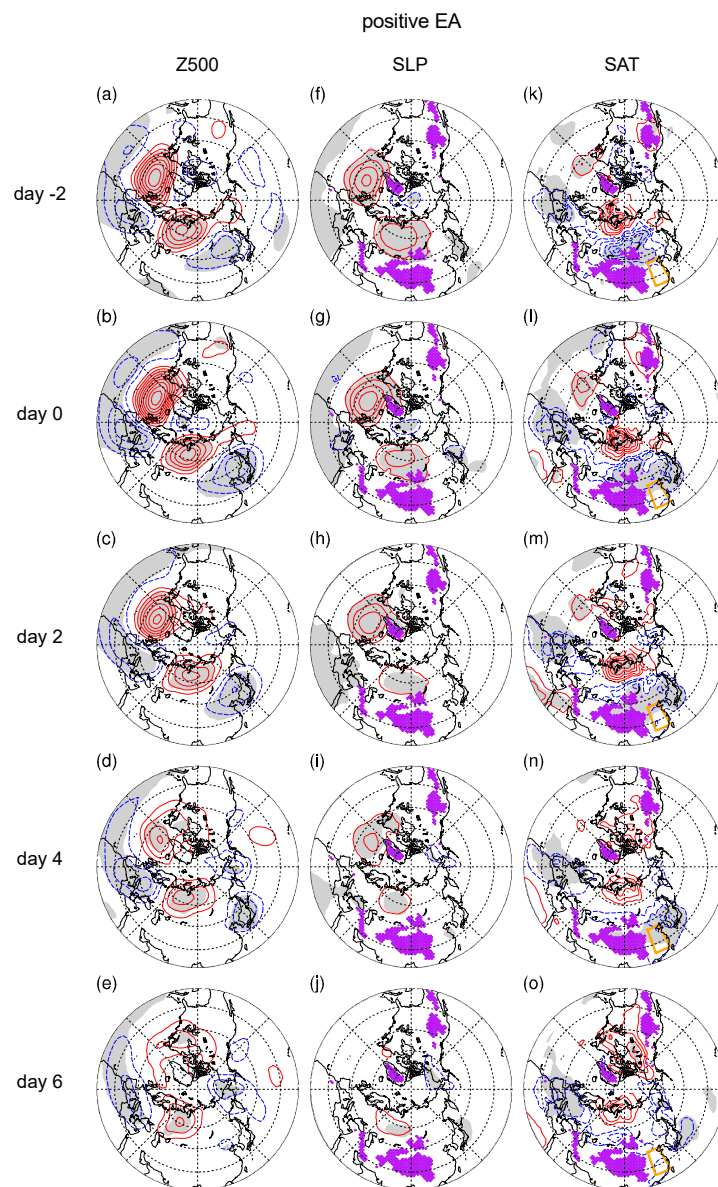


Figure 5. (a–o) Same as subfigures (a–o) of Figure 4, respectively, but for 51 positive EA events. Threshold values for the significance level p_{FDR}^* are 0.006, 0.005, and 0.004 for composites of anomalous Z500, SLP, and SAT, respectively.

3.3.3. SCA Events

For positive SCA events, at day -2 , wave train anomalies are evident from the northern North Atlantic to the region around Lake Baikal, with the strongest Z500 anomaly centered at the Barents Sea (Figure 6a). In fact, significant wave train anomalies appear at day -4 (not shown). The prominent positive SLP anomaly occurs over western Russia and the Scandinavian Peninsula (Figure 6f), facilitating the formation of the dipole pattern of SAT anomalies with the warm anomaly over the Arctic sea and the cold one over the region to the northwest of Lake Baikal (Figure 6k). At day 0, both the wave train anomalies at 500 hPa (Figure 6b) and the primary positive SLP anomaly over the Scandinavian peninsula/western Russia (Figure 6g) are enhanced. The negative SAT anomalies expand in the zonal direction but are still confined to the north of 45° N (Figure 6l). After day 0, both the Z500 anomalies and the positive SLP anomalies gradually weaken, but they are still significant until day 4. During this period, significant SAT anomalies persistently anchor over the mid-latitude Eurasian continent and show a tendency to penetrate southward to southern China (Figure 6m,n). At day 6,

both the primary positive Z500 anomaly and the primary SLP anomaly retrograde northwestward (Figure 6e,j). In addition, some positive SLP anomalies that are detached from the primary SLP anomaly over the Scandinavian peninsula/western Russia move eastward and become significant over northeastern China (Figure 6j). After day 6, only marginally significant circulation anomalies could be observed (not shown).

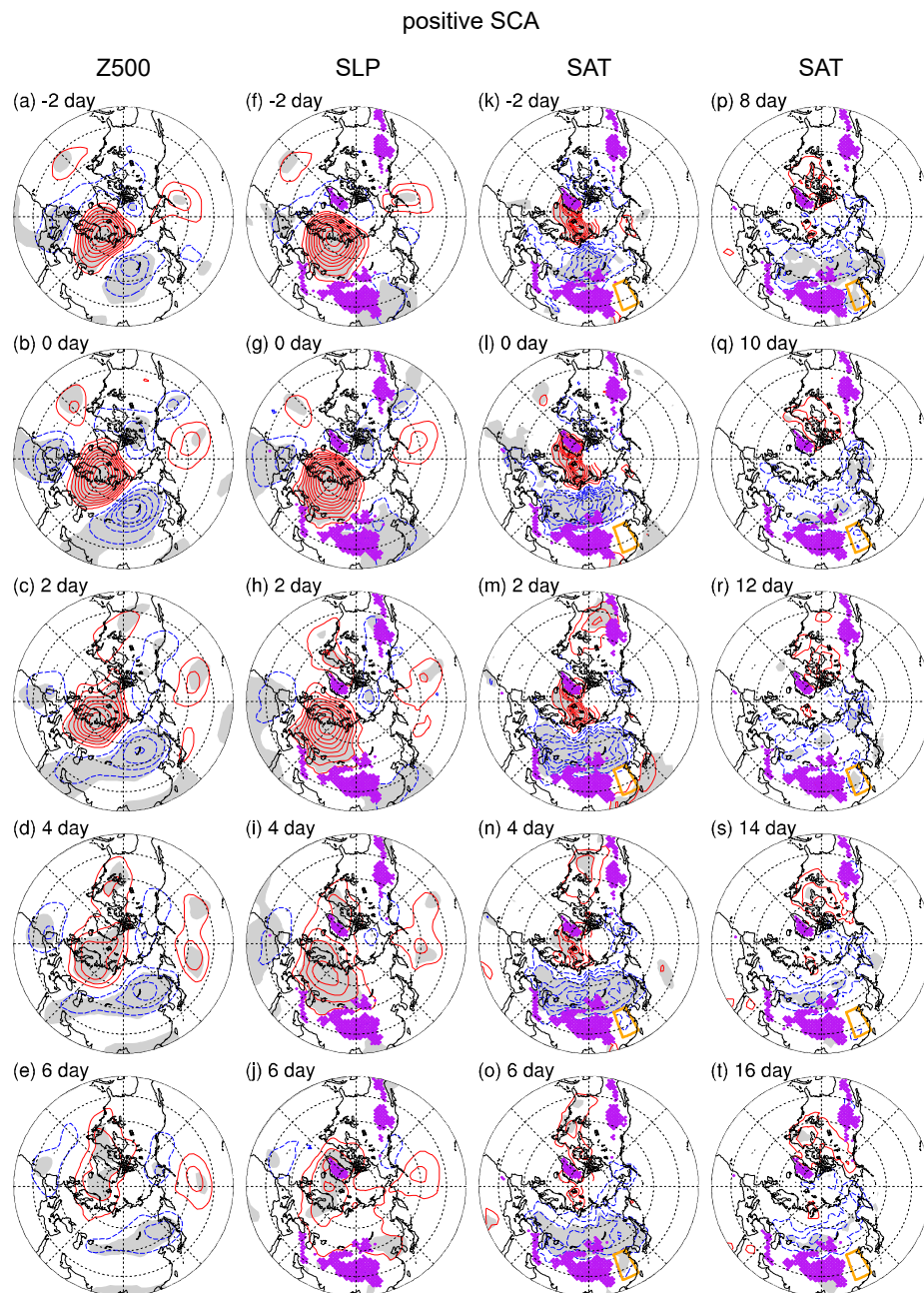


Figure 6. (a–o) Same as subfigures (a–o) of Figure 4, respectively, but for 61 positive SCA events; (p–t) the fourth column is composite SAT anomalies from day 8 to day 16, with an interval of 2 days, for 61 positive SCA events. Days relative to peak days of positive SCA events are indicated in the top left of each panel. Threshold values for the significance level p_{FDR}^* are 0.005, 0.003, and 0.003 for the composites of anomalous Z500, SLP, and SAT, respectively.

At day 6 (Figure 6o), interestingly, negative SAT anomalies over the mid-latitude Eurasian continent are still significant. Until day 12 (Figure 6p–r), the negative SAT anomalies continuously propagate

southeastward along the edge of the Tibetan Plateau to influence southern China. This southeastward propagation of SAT anomalies is similar to that in the EA events (Figure 5l–n).

Like EA events, negative SCA events also exhibit a similar evolution but with the opposite sign to their positive counterparts (not shown). Specifically, positive SAT anomalies first form over the mid-latitude Eurasian continent before day 5, and then propagate southeastward to significantly influence southern China until day 12.

Therefore, significant SAT anomalies are first induced and accumulate over the mid-latitude Eurasian continent during the first 5-day period after the peak day of SCA events. After day 6, although the typical circulation features of SCA events almost disappear, SAT anomalies were able, by themselves, to gradually propagate southeastward along the edge of the Tibetan Plateau to influence southern China, accounting for the formation of significant SAT anomalies at the subsequent 6-day period shown in Figures 2f and 3f.

3.3.4. EAWR Events

Positive EAWR events are characterized by stationary wave train anomalies along the mid- and high-latitude Eurasian continent, from the northeast Pacific to the Ural Mountains. Wave train anomalies become evident at day -4 (not shown) and are enhanced from day -2 to day 0 (Figure 7a,b).

Correspondingly, significant positive and negative SLP anomalies are enhanced over western Europe and Central Asia, respectively (Figure 7f,g). Significant positive SAT anomalies occur between the dipole SLP anomalies over Eurasia, while the significant negative SAT anomaly is mainly confined to the northern rim of the Tibetan Plateau at day 0 (Figure 7l).

From day 0 to day 4, negative Z500 anomalies over East Asia become significant, while Z500 anomalies upstream of the primary positive Z500 anomalies around the Ural Mountains gradually weaken and become insignificant (Figure 7b–d), indicating the propagation of stationary Rossby waves among these anomaly centers [12]. At day 6, only the positive Z500 anomalies over the Ural Mountains are significant (Figure 7e).

Corresponding to the persistence of positive Z500 anomalies over the Ural Mountains, the positive SLP anomaly persists around the Ural Mountains until day 6 (Figure 7f–i). As in the positive EA events, the positive SLP anomaly also indicates the enhancement of the northwestern part of the Siberian high. However, in contrast to positive EA events, positive SLP anomalies associated with positive EAWR events exhibit a northeast–southwest tilt (Figure 7f–i), contributing to the dipole pattern of the SAT anomaly with a northeast–southwest tilt over the Eurasian continent (Figure 7k–m). Negative SAT anomalies tend to occur over East Asia south of 60° N. In addition, the negative Z500 anomaly over East Asia (Figure 7c,d) might correspond to the deepening of the East Asia trough, which is also favorable for conducting cold air from the north to propagate southward. At day 2 and day 4 (Figure 7m,n), significant negative SAT anomalies propagate southward along the eastern slope of the Tibetan Plateau and influence southern China. At day 6, significant SAT anomalies continue to propagate southward and gradually move out of southern China (Figure 7o). As for the significance event after day 6 of the SAT anomaly shown in Figure 2i, it might be associated with the smoothing process, i.e., area-averaging the SAT over southern China, which might effectively reduce the case-to-case variability.

The negative EAWR events also show a similar daily evolution to their positive counterparts and induce significant positive SAT anomalies from approximately day 0 to day 4 (not shown). Therefore, the EAWR events also induce the significant SAT anomaly mainly during the first 5-day period after their peak days.

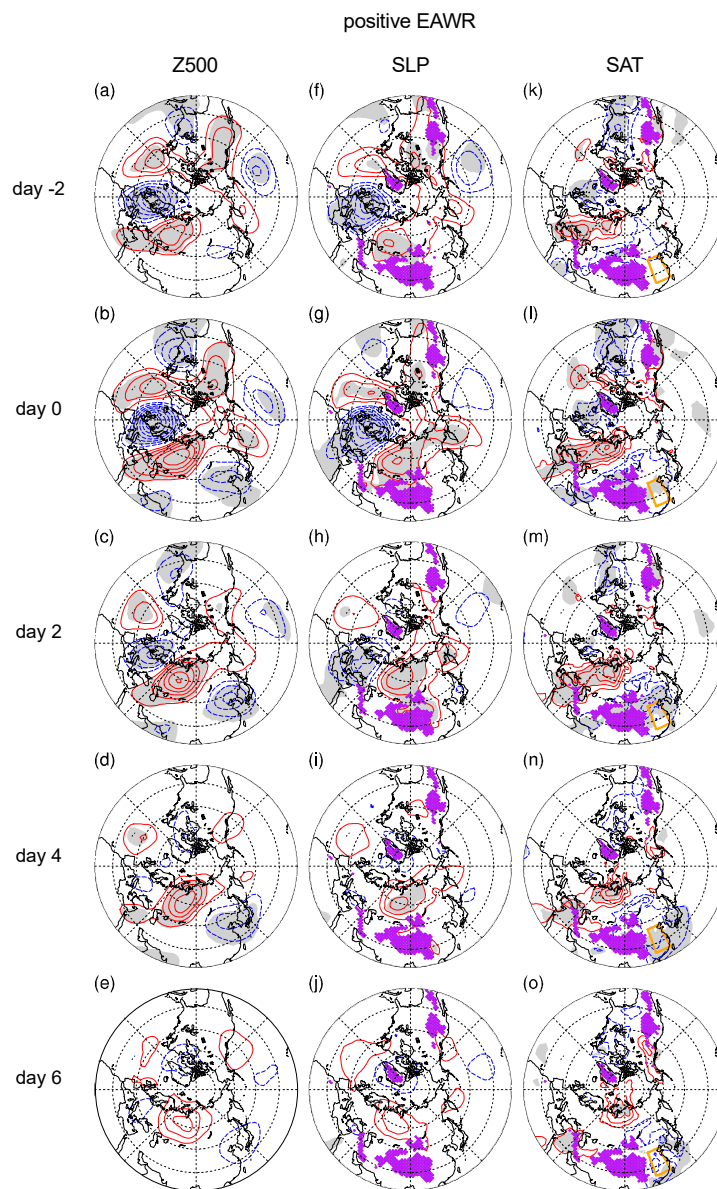


Figure 7. (a–o) Same as subfigures (a–o) of Figure 4, respectively, but for 64 positive EAWR events. Threshold values for the significance level p_{FDR}^* are 0.005, 0.003, and 0.003 for the composites of anomalous Z500, SLP, and SAT, respectively.

4. Discussion

Both the southward propagation of SAT anomalies from northern China in the positive WP events (Figure 4l–n) and the southeastward propagation of SAT anomalies from the northeastern Tibetan Plateau in the EA events (Figure 5k–n), the SCA events (Figure 6n–r) and EAWR events (Figure 7l–n) can be understood from the potential vorticity (PV) perspective. According to the conservativeness of PV, a negative anomaly of the potential temperature near the surface (or positive PV disturbance) can induce anticyclonic circulation [41]. Figure 8 shows the climatological mean 1000 hPa air temperature over East Asia, which is equal to the climatological mean 1000 hPa potential temperature. The background potential temperature shows an overall southwestward gradient direction, with a clockwise rotation when approaching southern China. Under such a background potential temperature, once the anticyclonic circulation is induced to the northeast of the Tibetan Plateau, it can advect the cold (warm) background potential temperature southwestward (northeastward), leading to a southeastward/southward propagation of the negative potential temperature anomaly

along the northeastern slope of the plateau, which acts as propagation of the thermal Rossby wave [18]. Overall, the southeastward/southward propagation of the SAT anomaly over East Asia is analogous to the westward propagation of the Rossby wave in the mid- and upper troposphere, which is embedded in the northward gradient of the background potential vorticity. Nevertheless, future study on PV invertibility is still needed to confirm the above speculation.

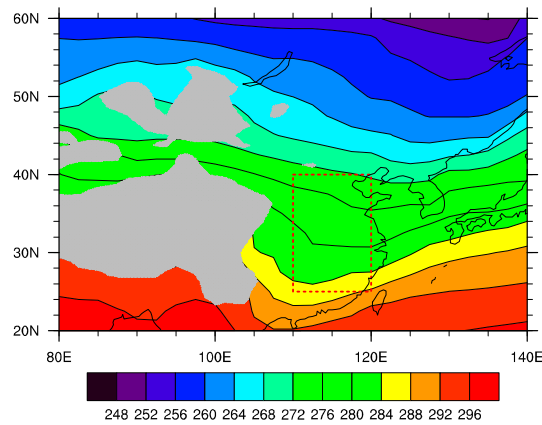


Figure 8. Forty-year climatological mean of winter (November to March) 1000 hPa air temperature (K). Dashed red rectangle represents southern China; gray shading represents topographic height exceeding 1500 m.

As revealed in the present study, positive WP events, EA events, SCA events, and EAWR events during the period 1979 to 2018 induced significant SAT anomalies over southern China. It is natural to ask whether these events have long-term variation in their occurrence frequency and influence.

Figure 9 shows the long-term frequency variation of the influential teleconnection events, based on the three reanalysis datasets. The frequency was 9-year-running smoothed to emphasize the long-term variation.

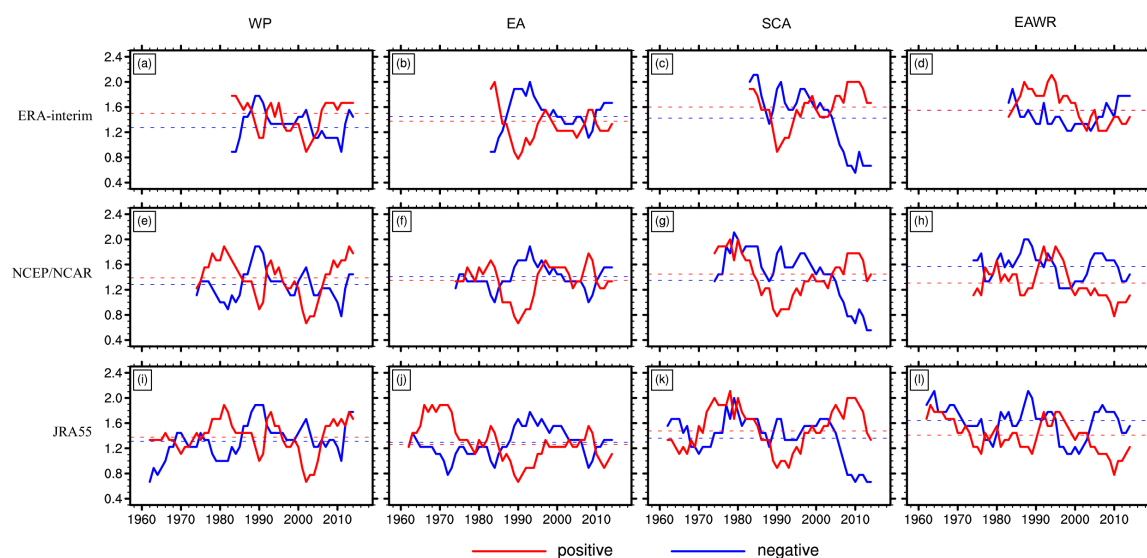


Figure 9. Nine-year running mean of the frequency of four teleconnection patterns, as revealed in ERA-interim (upper row), NCEP/NCAR (middle row), and JRA (lower row). Red (blue) lines represent the frequency of teleconnection patterns in their positive (negative) phase. The horizontal dashed red (blue) lines represent the mean frequency of the positive (negative) teleconnection patterns over the periods covered by the reanalysis datasets.

Overall, the different datasets exhibit similar frequency variations of these events over the common period 1979 to 2018, especially for WP, EA, and SCA events. Different datasets consistently reveal that positive WP and SCA events became more frequent after approximately 2005, while negative SCA events and positive EAWR events became less frequent after 2005 and 2000, respectively. This means that positive WP and SCA events (negative SCA events) had more influence on negative (positive) SAT anomalies over southern China after 2005. In contrast, positive EAWR events had less influence on negative SAT anomalies. Note that the recent more (less) frequent occurrence of positive (negative) SCA events revealed here is basically consistent with the more frequent occurrence of Scandinavian blocking after 2000 [42].

Note that, in addition to recent decades, positive SCA events also tended to occur frequently over the 1970s and 1980s (Figure 9g,k). If the recent Arctic Sea ice loss can account for the dramatic decrease in the occurrence of negative SCA events and the increase in positive SCA events after 2005 [42], there must be other dynamic mechanisms responsible for the relative increase in the frequency of positive SCA events over the 1970s and 1980s, since the Arctic Sea ice did not decline dramatically during those years. In addition, the occurrence frequency of positive SCA events seems to be out of phase with that of positive EAWR events (Figure 9g,h,k,l), and the occurrence frequency of EA events also shows evident decadal variation before 2000 (Figure 9b,f,j). These issues deserve further study.

Based on the JRA reanalysis data, all of these teleconnection events exhibit evident decadal variation. In fact, all the events that occurred before 1979 were also composited for each type of teleconnection event. After removing the linear trend during the period 1958 to 2018 at every grid point, the results show that circulation anomalies did not change qualitatively (not shown), indicating that the subseasonal variation and the influence of teleconnection events did not change qualitatively.

Some studies have noted that teleconnection events under some particular conditions could have more influence on the surface climate than others. For example, SCA-related anticyclonic events with evident eastward movement could induce extreme cold SAT anomalies over southern China [29]; WP patterns that arise from the PNA pattern of the same polarity have the most influence on North American near-surface and polar stratospheric air temperatures [43]. In addition, Luo et al. [44] pointed out that Ural blocking related to a positive NAO event is more favorable for the occurrence of the warm Arctic–cold Eurasian pattern. Inspired by these studies, it might be meaningful to further classify teleconnection events of the same type by considering their differences, which would help to extract more useful precursory signals for the formation of SAT anomalies over southern China.

5. Conclusions

This study utilized daily fields from three reanalysis datasets to explore the subseasonal influence of nine teleconnection patterns on the SAT over southern China. Due to the similar results obtained, the ensemble mean of the three reanalysis datasets was mainly used in the present study. The composite results show that positive WP, EA, SCA, and EAWR events induced significant negative SAT anomalies over southern China, while negative EA, SCA, and EAWR events induced significant positive SAT anomalies. Therefore, the linearity in the influence is evident for EA, SCA, and EAWR events. Significant SAT anomalies correspond to approximately 75% of the teleconnection events with the same sign.

Significant SAT anomalies over southern China induced by positive WP events, EA, and EAWR events mainly occurred during the first 5-day period after the peak day of these teleconnection events. However, there are fundamental differences in the evolution of the circulation anomalies between positive WP events and either positive EA or EAWR events. Positive WP events are generally associated with the westward development of a dipole Z500 anomaly over the northern Pacific, while positive EA and EAWR events develop from stationary wave train anomalies across the mid- and high latitudes in the Northern Hemisphere with a primary anticyclonic height anomaly over the Ural Mountains. Positive WP events are similar to the “Pacific” origin of the amplification of the Siberian high [18,19], while positive EA and EAWR events are similar to the “Atlantic” origin of the Siberian high [18,19].

In contrast, SCA events in both positive and negative phases induced significant SAT anomalies approximately 5 to 12 days after their peak day. Such long-lagged influence is achieved through inducing large-scale accumulation of cold anomalies over the mid-latitude Eurasian continent before day 5, and the subsequent southeastward propagation of SAT anomalies by themselves as a surface thermal Rossby wave along the northeastern slope of the Tibetan Plateau after day 5.

Our results are useful for subseasonal prediction of persistent SAT anomalies over southern China. On the one hand, significant circulation anomalies of the four teleconnection patterns generally begin to appear at least 4 days before their peak days. On the other hand, significant SAT anomalies generally persist after the peak days of the four teleconnection patterns. Therefore, taking SCA events as an example, if day −4 (4 days before the peak day) is regarded as the starting day at which Z500 anomalies become significant and day 8 (8 days after the peak day) is regarded as the middle of a 6-day period during which SAT anomalies persist over southern China, there is a 12-day time interval between precursor circulation anomalies and SAT anomalies. For the other three patterns, there is generally a 6-day time interval. Such time intervals indicate that the four teleconnection patterns could be used as subseasonal predictors for SAT anomalies over southern China.

Author Contributions: Conceptualization, N.S. Writing—initial draft, N.S. Writing—review and editing, N.S., D.Z., and Y.W. Investigation, N.S., D.Z., Y.W., and S.T.

Funding: This work was jointly supported by the National Key R&D Program of China (Grant No. 2016YFA0600702), the Chinese Natural Science Foundation (41575057 and 41975063), and the Funding of Jiangsu Innovation and Entrepreneurship Team.

Acknowledgments: The National Center for Atmospheric Research NCAR Command Language (NCL) was used to perform the calculations and draw the plots.

Conflicts of Interest: The authors declare no conflict of interest.

References

- Wallace, J.M.; Gutzler, D.S. Teleconnections in the geopotential height field during the Northern Hemisphere winter. *Mon. Weather Rev.* **1981**, *109*, 784–812. [[CrossRef](#)]
- Horel, J. A rotated principal component analysis of the interannual variability of the Northern Hemisphere 500 mb height field. *Mon. Weather Rev.* **1981**, *109*, 2080–2092. [[CrossRef](#)]
- Barnston, A.G.; Livezey, R.E. Classification, Seasonality and Persistence of Low-Frequency Atmospheric Circulation Patterns. *Mon. Weather Rev.* **1987**, *115*, 1083–1126. [[CrossRef](#)]
- Lau, N.-C. Variability of the observed midlatitude storm tracks in relation to low-frequency changes in the circulation pattern. *J. Atmos. Sci.* **1988**, *45*, 2718–2743. [[CrossRef](#)]
- Athanasiadis, P.J.; Wallace, J.M.; Wettstein, J.J. Patterns of wintertime jet stream variability and their relation to the storm tracks. *J. Atmos. Sci.* **2010**, *67*, 1361–1381. [[CrossRef](#)]
- Blackmon, M.L.; Lee, Y.H.; Wallace, J.M. Horizontal structure of 500 mb height fluctuations with long, intermediate and short time scales. *J. Atmos. Sci.* **1984**, *41*, 961–980. [[CrossRef](#)]
- Nakamura, H.; Tanaka, M.; Wallace, J.M. Horizontal structure and energetics of Northern Hemisphere wintertime teleconnection patterns. *J. Atmos. Sci.* **1987**, *44*, 3377–3391. [[CrossRef](#)]
- Frederiksen, J.S. A unified three-dimensional instability theory of the onset of blocking and cyclogenesis. II: Teleconnection patterns. *J. Atmos. Sci.* **1983**, *40*, 2593–2609. [[CrossRef](#)]
- Simmons, A.J.; Wallace, J.M.; Branstator, G.W. Barotropic Wave Propagation and Instability, and Atmospheric Teleconnection Patterns. *J. Atmos. Sci.* **1983**, *40*, 1363–1392. [[CrossRef](#)]
- Feldstein, S.B. Fundamental mechanisms of the growth and decay of the PNA teleconnection pattern. *Quart. J. Roy. Meteor. Soc.* **2002**, *128*, 775–796. [[CrossRef](#)]
- Tanaka, S.; Nishii, K.; Nakamura, H. Vertical structure and energetics of the Western Pacific teleconnection pattern. *J. Clim.* **2016**, *29*, 6597–6616. [[CrossRef](#)]
- Hoskins, B.J.; Karoly, D.J. The steady linear response of a spherical atmosphere to thermal and orographic forcing. *J. Atmos. Sci.* **1981**, *38*, 1179–1196. [[CrossRef](#)]
- Bueh, C.; Nakamura, H. Scandinavian pattern and its climatic impact. *Quart. J. Roy. Meteor. Soc.* **2007**, *133*, 2117–2131. [[CrossRef](#)]

14. Tan, B.; Yuan, J.; Dai, Y.; Feldstein, S.B.; Lee, S. The linkage between the Eastern Pacific teleconnection pattern and convective heating over the tropical Western Pacific. *J. Clim.* **2015**, *28*, 5783–5794. [[CrossRef](#)]
15. Branstator, G. The Maintenance of Low-Frequency Atmospheric Anomalies. *J. Atmos. Sci.* **1992**, *49*, 1924–1946. [[CrossRef](#)]
16. Wang, N.; Zhang, Y. Evolution of Eurasian teleconnection pattern and its relationship to climate anomalies in China. *Clim. Dyn.* **2014**, *44*, 1017–1028. [[CrossRef](#)]
17. Zhang, Y.; Sperber, K.R.; Boyle, J.S. Climatology and Interannual Variation of the East Asian Winter Monsoon: Results from the 1979–95 NCEP/NCAR Reanalysis. *Mon. Weather Rev.* **1997**, *125*, 2605–2619. [[CrossRef](#)]
18. Takaya, K.; Nakamura, H. Mechanisms of Intraseasonal Amplification of the Cold Siberian High. *J. Atmos. Sci.* **2005**, *62*, 4423–4440. [[CrossRef](#)]
19. Takaya, K.; Nakamura, H. Geographical Dependence of Upper-Level Blocking Formation Associated with Intraseasonal Amplification of the Siberian High. *J. Atmos. Sci.* **2005**, *62*, 4441–4449. [[CrossRef](#)]
20. Gong, D.; Wang, S.; Zhu, J. East Asian winter monsoon and Arctic Oscillation. *Geophys. Res. Lett.* **2001**, *28*, 2073–2076. [[CrossRef](#)]
21. Takaya, K.; Nakamura, H. Interannual Variability of the East Asian Winter Monsoon and Related Modulations of the Planetary Waves. *J. Clim.* **2013**, *26*, 9445–9461. [[CrossRef](#)]
22. Wang, L.; Chen, W. An Intensity Index for the East Asian Winter Monsoon. *J. Clim.* **2014**, *27*, 2361–2374. [[CrossRef](#)]
23. Cheung, H.H.N.; Zhou, W. Simple Metrics for Representing East Asian Winter Monsoon Variability: Urals Blocking and Western Pacific Teleconnection Patterns. *Adv. Atmos. Sci.* **2016**, *33*, 695–705. [[CrossRef](#)]
24. Feldstein, S.B. The timescale, power spectra, and climate noise properties of teleconnection patterns. *J. Clim.* **2000**, *13*, 4430–4440. [[CrossRef](#)]
25. Yuan, J.; Tan, B.; Feldstein, S.B.; Lee, S. Wintertime North Pacific Teleconnection Patterns: Seasonal and Interannual Variability. *J. Clim.* **2015**, *28*, 8247–8263. [[CrossRef](#)]
26. Ding, Y. Build-up, air mass transformation and propagation of Siberian high and its relations to cold surge in East Asia. *Meteorol. Atmos. Phys.* **1990**, *44*, 281–292. [[CrossRef](#)]
27. Liu, Y.; Lin, W.; Wen, Z.; Wen, C. Three Eurasian teleconnection patterns: Spatial structures, temporal variability, and associated winter climate anomalies. *Clim. Dyn.* **2014**, *42*, 2817–2839. [[CrossRef](#)]
28. Zhou, W.; Chan, J.C.L.; Chen, W.; Ling, J.; Pinto, J.G.; Shao, Y. Synoptic-Scale Controls of Persistent Low Temperature and Icy Weather over Southern China in January 2008. *Mon. Weather Rev.* **2009**, *137*, 3978–3991. [[CrossRef](#)]
29. Bueh, C.; Shi, N.; Xie, Z. Large-scale circulation anomalies associated with persistent low temperature over Southern China in January 2008. *Atmos. Sci. Lett.* **2011**, *12*, 273–280. [[CrossRef](#)]
30. Peng, J.B.; Bueh, C. Precursory Signals of Extensive and Persistent Extreme Cold Events in China. *Atmos. Ocean. Sci. Lett.* **2012**, *5*, 252–257.
31. Hsu, H.-H. Propagation of Low-Level Circulation Features in the Vicinity of Mountain Ranges. *Mon. Weather Rev.* **1987**, *115*, 1864–1893. [[CrossRef](#)]
32. Dee, D.P.; Uppala, S.M.; Simmons, A.J.; Berrisford, P.; Poli, P.; Kobayashi, S.; Andrae, U.; Balmaseda, M.A.; Balsamo, G.; Bauer, P.; et al. The ERA-Interim reanalysis: Configuration and performance of the data assimilation system. *Quart. J. Roy. Meteor. Soc.* **2011**, *137*, 553–597. [[CrossRef](#)]
33. Kalnay, E.; Kanamitsu, M.; Kistler, R.; Collins, W.; Deaven, D.; Gandin, L.; Iredell, M.; Saha, S.; White, G.; Woollen, J.; et al. The NCEP/NCAR 40-year reanalysis project. *Bull. Amer. Meteor. Soc.* **1996**, *77*, 437–470. [[CrossRef](#)]
34. Kobayashi, S.; Ota, Y.; Harada, Y.; Ebata, A.; Moriya, M.; Onoda, H.; Onogi, K.; Kamahori, H.; Kobayashi, C.; Endo, H.; et al. The JRA-55 Reanalysis: General Specifications and Basic Characteristics. *J. Meteorol. Soc. Jpn.* **2015**, *93*, 5–48. [[CrossRef](#)]
35. Yang, S.; Lau, K.M.; Kim, K.M. Variations of the East Asian Jet Stream and Asian-Pacific-American Winter Climate Anomalies. *J. Clim.* **2002**, *15*, 306–325. [[CrossRef](#)]
36. Baldwin, M.P.; Dunkerton, T.J. Stratospheric Harbingers of Anomalous Weather Regimes. *Science* **2001**, *294*, 581–584. [[CrossRef](#)] [[PubMed](#)]
37. Wilks, D.S. “The Stippling Shows Statistically Significant Grid Points”: How Research Results are Routinely Overstated and Overinterpreted, and What to Do about It. *Bull. Amer. Meteor. Soc.* **2016**, *97*, 2263–2273. [[CrossRef](#)]

38. Walker, G.T.; Bliss, E.W. World weather V. *Mem. Roy. Meteor. Soc.* **1932**, *4*, 53–84.
39. Rogers, J.C. The North Pacific Oscillation. *J. Climate* **1981**, *1*, 39–57. [[CrossRef](#)]
40. Linkin, M.E.; Nigam, S. The North Pacific Oscillation–West Pacific Teleconnection Pattern: Mature-Phase Structure and Winter Impacts. *J. Clim.* **2008**, *21*, 1979–1997. [[CrossRef](#)]
41. Hoskins, B.J.; McIntyre, M.E.; Robertson, A.W. On the use and significance of isentropic potential vorticity maps. *Quart. J. Roy. Meteor. Soc.* **1985**, *111*, 877–946. [[CrossRef](#)]
42. Crasemann, B.; Handorf, D.; Jaiser, R.; Dethloff, K.; Nakamura, T.; Ukita, J.; Yamazaki, K. Can preferred atmospheric circulation patterns over the North-Atlantic-Eurasian region be associated with arctic sea ice loss? *Polar Sci.* **2017**, *14*. [[CrossRef](#)]
43. Dai, Y.; Tan, B. Two Types of the Western Pacific Pattern, Their Climate Impacts, and the ENSO Modulations. *J. Clim.* **2019**, *32*, 823–841. [[CrossRef](#)]
44. Luo, D.; Xiao, Y.; Diao, Y.; Dai, A.; Franzke, C.L.E.; Simmonds, I. Impact of Ural Blocking on Winter Warm Arctic–Cold Eurasian Anomalies. Part II: The Link to the North Atlantic Oscillation. *J. Clim.* **2016**, *29*, 3949–3971. [[CrossRef](#)]



© 2019 by the authors. Licensee MDPI, Basel, Switzerland. This article is an open access article distributed under the terms and conditions of the Creative Commons Attribution (CC BY) license (<http://creativecommons.org/licenses/by/4.0/>).